JOURNAL OF MATERIALS SCIENCE **39** (2004) 6687–6704

Characterisation of fine-grained oxide ceramics

G. D. WEST, J. M. PERKINS, M. H. LEWIS
Centre for Advanced Materials, Department of Physics, University of Warwick, Coventry, CV4 7AL, UK
E-mail: g.west@lboro.ac.uk

A range of high resolution techniques have been used to characterise the grain boundary segregation behaviour of rare earth (RE) doped (La, Gd, Eu and Yb) alumina and spinel. TEM based techniques (HR-TEM, HAADF STEM and EDS) have been used to study the structure and chemistry of grain boundaries. The use of a HAADF detector in STEM provides atomic number contrast and easy identification of heavy (RE) segregants. This has been used to produce high resolution RE elemental maps, showing the width of the segregated region to be less than the size of the electron probe (1 nm) for all boundaries studied. EDS showed that within a 1 nm thick boundary region (an upper limit) the RE cations would account for 10 (±2)% and 15 (±2)% of the cation total in alumina and spinel respectively. Preliminary results from ultra-high resolution STEM (probe size ~0.1 nm) suggest that, in spinel, the segregated region is actually composed of a much thinner continuous monolayer of RE atoms at the grain boundary. This is consistent with HR-TEM, which showed spinel grain boundaries possessed minimal grain boundary structural disorder.

AFM has been used to study the effect of RE grain boundary segregation on thermal grooving behaviour. The improvement in resolution that is achieved by operating in Tapping™ mode is shown to translate into an improved profile of the groove root. This has been used in conjunction with Electron Backscattered Diffraction (EBSD) to examine the relationship between grain boundary geometry and misorientation. The addition of RE dopants to alumina was found to significantly increase the size of grain boundary grooves. This can be attributed to the out-diffusion of RE segregants, an effect which compromises grain boundary energy calculations for materials with grain boundary segregation. AFM and EBSD are also used to relate anisotropic tribo-chemical polishing-wear with grain orientation.

1. Introduction

The microstructural evolution during sintering of alumina is well known to be highly sensitive to low levels of impurities. This has led to the production of ultra high purity starting powders and the formulation of clean processing procedures. These inconveniences are however more than compensated by the microstructural control that dopants can provide. A classic example is the addition of MgO to alumina, which, under appropriate sintering conditions, increases density by reducing pore/grain boundary separation. This discovery in the 1960s led to the development and commercialisation of translucent alumina (Lucalox™) for the containment of corrosive plasma in high-pressure sodium lamps, still used extensively for street lighting. The optical quality attainable in coarse-grained polycrystalline alumina is however severely limited by grain boundary scattering, which is inherent to non-cubic materials.

The optical properties of polycrystalline alumina have attracted renewed interest recently, triggered by the observation that decreases in grain size yield improvements in optical quality [1]. This behaviour is counter-intuitive as decreasing the grain size increases the number of grain boundaries from which scattering can occur. The phenomenon has been explained by a change in scattering mechanism as the grain size becomes comparable with the wavelength of light [2]. The improvement in optical quality that can be achieved simply by reducing grain size is illustrated in Fig. 1. The fine-grained alumina possesses a much greater unscattered transmitted component compared with the coarse-grained alumina (similar to Lucalox™) and leads to the possibility of producing a genuinely transparent material.

These improvements in optical quality are additive to the well-known increases in hardness, wear resistance and strength that can be achieved as grain size is decreased [3]. Fig. 2 shows a clear increase in hardness with decreasing grain size for both alumina and spinel.

The improvements in mechanical and optical properties provide a strong motivation for decreasing the grain size in alumina and ceramics in general. However, to achieve the available improvements, porosity and other

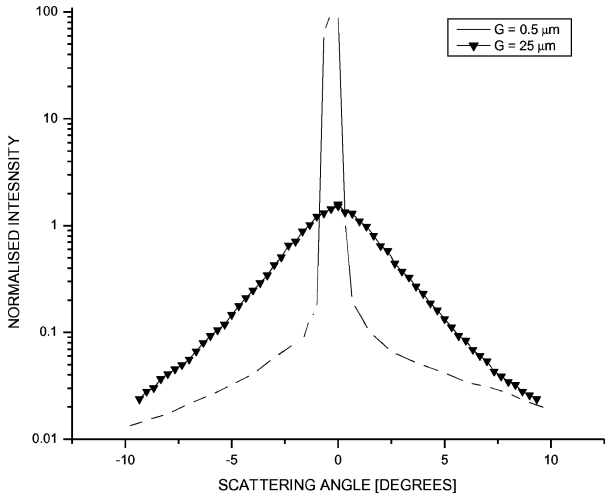

Figure 1 The angular distribution of light ($\lambda = 633$ nm) scatter around the forward direction for fine ($G = 0.5\ \mu$m) and coarse ($G = 25\ \mu$m) grained alumina (both samples ~ 0.5 mm thick).

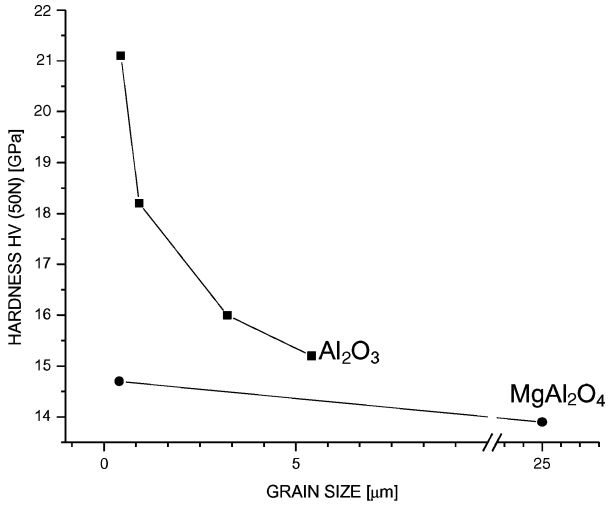

Figure 2 The relationship between grain size and hardness for alumina and spinel.

defects must be avoided, requiring the optimisation of processing and sintering procedures. The grain size of undoped alumina sintered using such procedures is known to be highly sensitive to sintering temperature and it is difficult to restrict grain growth. The sensitivity can be reduced by the addition of dopants (e.g., Zr, Y and other rare earths), which inhibit grain growth by reducing the diffusivity of cations at grain boundaries. The same process is also responsible for the large (up to 3 orders of magnitude) increase in creep resistance [4, 5], which provides an additional motivation for studying these materials.

An alternative ceramic that combines high hardness with optical transparency is magnesium aluminate spinel. Although the addition of dopants to spinel has not been systematically investigated, it is considered considerably less sensitive to low levels of impurities than alumina [6]. Despite this, low levels of certain impurities (e.g., Ti) can alter the defect population within the cation lattice and promote abnormal grain growth. Sintering behaviour is also a strong function of spinel stoichiometry ($MgO{\cdot}nAl_2O_3$) with boundary mobility 100–1000 times greater in Mg rich ($n < 1$) compared with Al rich ($n > 1$) compositions [6]. This is important if there is a variation in stoichiometry for example at a grain boundary. The motivation for decreasing the grain size in spinel is the improvement in mechanical properties that can be achieved, since in cubic ceramics optical quality is not intrinsically linked with grain size.

In this paper, the use of high-resolution microscopy to characterise fine-grained oxide ceramics is discussed. Together these techniques enable critical grain boundary properties such as structure, chemistry, energy and misorientation to be determined. This is a necessary requirement for furthering the understanding of sintering behaviour and mechanical and optical properties of these ceramics.

2. Experimental procedures

2.1. Sample preparation

Fully dense alumina and stoichiometric spinel (i.e., $MgAl_2O_4$) samples were prepared from Taimicron TM-DAR (Taimei Chemicals, Japan) and Baikowski S30CR (Baikowski Chimie, France) powders, respectively. Rare earth (RE) dopants (La, Gd, Eu and Yb) were introduced by dissolving the appropriate hydrated RE nitrate, e.g., 99.99% ytterbium (III) nitrate pentahydrate (Aldrich Chemicals, UK), in IPA and mixing with an alumina/IPA slurry. The slurry was dried at room temperature and used without further processing to minimise possible contamination. The powder was hot-pressed in a graphite die at temperatures between 1400 and 1650°C with a dwell time of 10 min and a pressure of 30 MPa. A dopant level of 500 ppm (RE: Al (or Al + Mg) cation ratio) was used, although grain boundary concentration was dependent on grain size and hence sintering temperature. All doped samples with an average grain size $>1\ \mu$m (i.e., $\geq$1500°C) contained precipitates, suggesting saturation of grain boundary segregants. The distribution of these precipitates was examined using SEM and found to be uniform. Unless stated otherwise all alumina samples described were prepared at 1500°C and all spinel samples at 1400°C.

2.2. Characterisation techniques

TEM was performed using a Jeol 2000 FX and a Philips Tecnai F20 FEG both operating at 200 kV. The latter is a hybrid TEM/STEM equipped with a high angle annular dark field detector (HAADF) (Model 3000, Fischione Instruments) and EDS (Oxford Link ISIS 300) and was used for both high resolution and analytical characterisations. In addition ultra-high resolution images of an Eu-doped spinel were obtained from the super-STEM facility, located at Daresbury, UK [7]. This dedicated STEM operates at 100 kV and is equipped with a spherical aberration corrector (Nion Co.). Images were acquired using a HAADF detector with a collection angle range between 70 and 210 mrads and an electron probe size of $\sim$1 Å. PEELS spectra were recorded at 2 Å intervals along lines of interest each with an acquisition time of 1 s. TEM sample preparation involved standard grinding and polishing procedures, followed by ion milling (Ar) to electron transparency using a Gatan PIPS system.

Initial electron backscattered diffraction (EBSD) experiments were conducted using a HKL Technology system attached to a Philips XL30 FEG SEM operating at 20 kV. Further work was performed using a TSL system attached to a Philips XL30 LaB_6 SEM. Samples were prepared by conventional grinding and polishing procedures followed by an extended finish with colloidal silica to removal all surface damage. To avoid charging, samples were lightly coated with either C or Au/Pd, the latter was found to produce strong EBSD patterns more reliably. Surface preparation and conductive coating deposition are both very important practical issues for EBSD of ceramics and are discussed in detail by Farrer *et al* [8]. Samples were tilted 70° to the horizontal and patterns were indexed using an α-Al_2O_3 structure file (i.e., trigonal, (D3d)(-3m), $a = 4.759$ Å, $c = 12.991$ Å). All data was analysed using commercial HKL Technology (Channel 5, Tango) and TSL (OIM analysis) software.

AFM was performed using a Digital Instruments module with a Nanoscope IIIa controller. The microscope was operated in both contact and tapping modes with Si_3N_4 and Si (TAP 300) tips respectively (both supplied by Lot-Oriel). In tapping mode oscillations were set near free amplitude (i.e., high set point). Indentations were used as reference marks so that specific areas (e.g., those previously examined with EBSD) could be located using a visible light microscope positioned directly above the AFM module. Samples were examined both before and after thermally etching at 1100°C for 2 h.

3. Results and discussion

3.1. The effect of rare earth dopants on microstructure

As expected, the addition of RE dopants to alumina reduced the grain size relative to undoped samples (Fig. 3). Typical microstructures of doped aluminas are shown in Fig. 4. The microstructures of undoped and Yb and Gd doped alumina were found to be equiaxed, whereas the addition of La can be seen to cause some grain elongation.

This grain elongation seems to suggest that grain boundary segregation is non-uniform, this will be discussed further in the succeeding sections.

The microstructural evolution with sintering temperature for undoped and RE doped spinel was complicated by poor compatibility with the graphite die. The use of refractory metal spacers such as Mo were found to react with RE to form the so-called metal bronzes. Consequently, both doped and undoped spinels were prepared at a single temperature of 1400°C, where these problems were minimised. Both doped and undoped samples were highly transparent, with a real in line transmission of over 75% [9]. Such transparency was due to the pore-free microstructure that these materials possessed (Fig. 5). Although the grain sizes of doped and undoped samples were similar, the addition of the RE dopant reduced the abnormal grain growth that occurred in the undoped sample, predominately at the edge. Abnormal grain growth has been reported

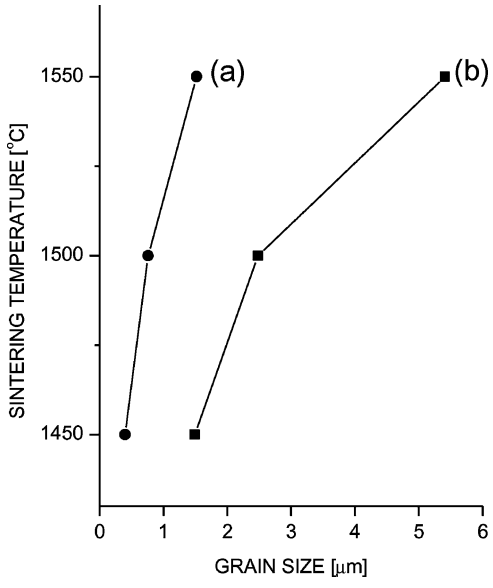

Figure 3 The relationship between hot pressing temperature and grain size for La-doped (a) and undoped (b) alumina.

previously [6] and could be due to local deviations in stoichiometry.

3.2. Characterising rare earth segregation

The segregation of RE cations to grain boundaries in alumina has been demonstrated using a variety of techniques such as SIMS [10], Auger [11] and those based on TEM (EDS, STEM, HR-TEM and PEELS) [12–15]. The detection of segregation is relatively straightforward, especially when there is such a large atomic number differential. For example, the segregation of RE cations to grain boundaries in doped alumina (or spinel) can be observed using a backscatter electron detector in an SEM. This is shown in Fig. 6b where there is a clear increase in grain boundary brightness compared with the undoped sample in Fig. 6a. The problem with this technique, and indeed many of the other techniques that have been used (SIMS, Auger and to a lesser extent EDS in STEM), is that they possess insufficient spatial resolution to provide a reliable measure of boundary width and hence boundary concentration. This is further complicated by difficulties aligning the boundaries into the edge on position, a necessity even for qualitative study. TEM is currently the only technique, which can overcome these difficulties satisfactorily.

3.3. Measuring the width of the segregated region using EDS

The segregation of rare earth cations to grain boundaries in oxide ceramics is simple to demonstrate using EDS in STEM (or TEM). An example is shown in Fig. 7 where the composition at a grain boundary (position 2) is compared with an intragranular region (position 1) for Yb doped spinel. In addition to Yb, S (the major impurity in the powder used) can also be seen to segregate to the grain boundary. Although it is straightforward to quantify the concentration of impurities detected in such spectra using the Cliff-Lorimer equation [16a],

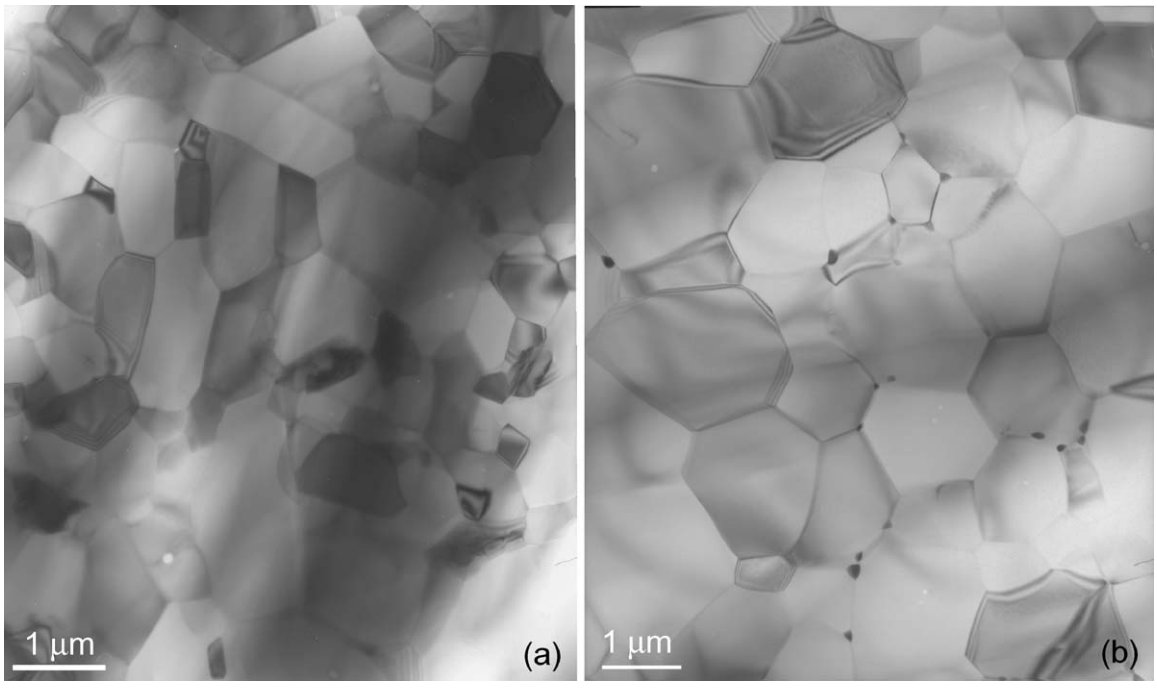

Figure 4 TEM micrographs of La-doped (a) and Gb-doped (b) alumina HPed at 1500°C.

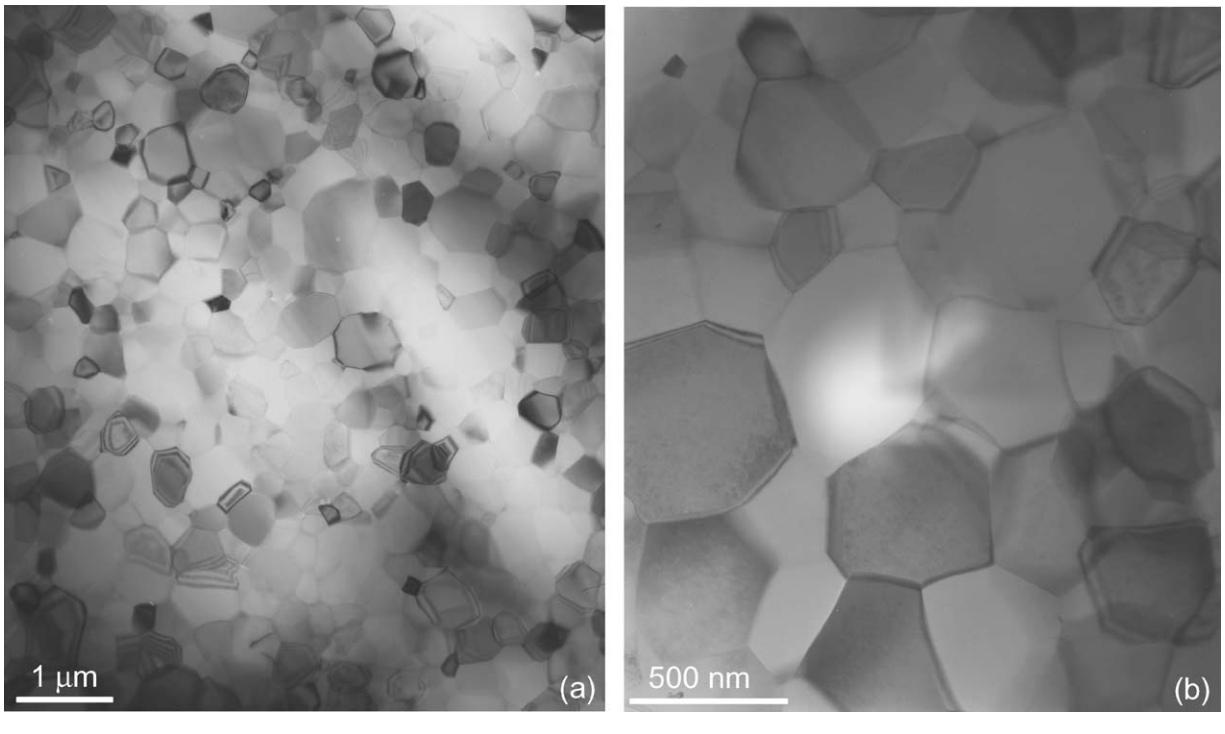

Figure 5 TEM micrographs of undoped (a) and Yb-doped (b) spinel HPed at 1400°C.

unless the width of the segregated region and the size of the electron probe are known precisely, the data is of limited use. The real problem is measuring the thickness of the RE segregated layer, which previous studies in alumina have suggested is ∼1 nm [15]. Attempts were made to perform EDS with very small probes but the counting statistics were poor, and the long acquisition times required were both inconvenient and increased the likelihood of practical problems such as drift, contamination and beam damage. As discussed in detail in the next section it was found to be more accurate (and convenient) to measure the width of the segregated region using HAADF STEM.

3.4. Measuring the width of the segregated region using HAADF STEM

In STEM the microscope is operated in diffraction mode so the collection angle of the HAADF detector can be controlled by adjusting the camera length. As shown in Fig. 8 the diffracted component of contrast within an image increases with increasing camera length. (It should be noted that genuine HAADF images contain no diffraction contrast and have collection angles >50 mrad). At collection angles >50 mrads image intensity is provided by Rutherford Scattering (i.e., electrons scattered by the nucleus, atomic number Z). This can be expressed using the differential Rutherford

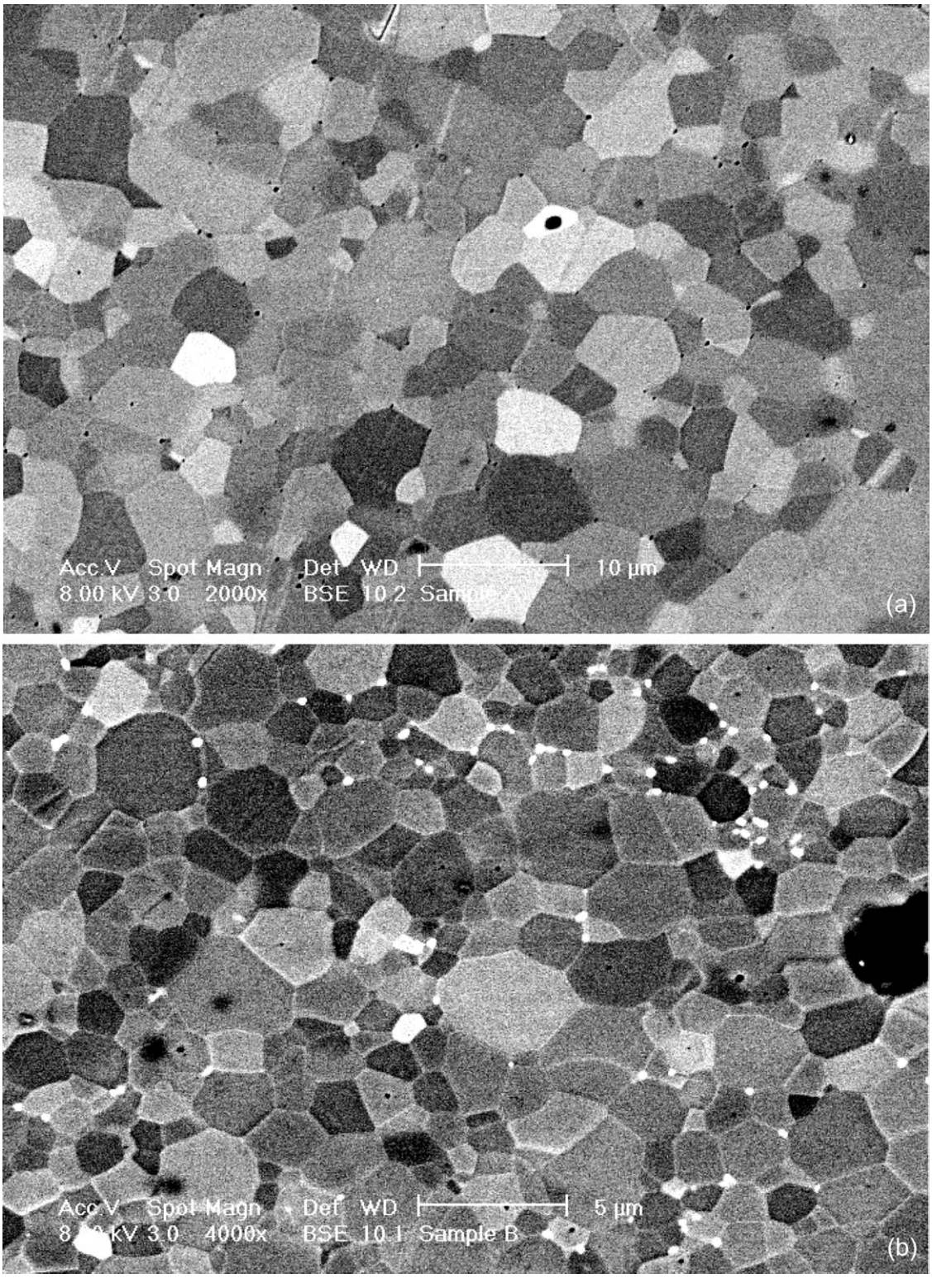

Figure 6 (BSE) SEM micrographs of undoped (a) and Yb doped (b) alumina (Courtesy of F. J. Humphreys and I. Brough).

cross section ($d\sigma/d\cos\theta$), given in Equation 1.

$$\left(\frac{d\sigma}{d\cos\theta}\right)_R = \frac{\pi}{2} Z^2 \alpha^2 \left(\frac{\hbar c}{KE}\right)^2 \frac{1}{(1-\cos\theta)^2} \quad (1)$$

where α is a dimensionless constant (=1/137), $\hbar = h/2\pi$ (h = Planck's constant), c = velocity of light, KE = energy of an electron, and θ = scattering angle.

This equation predicts that scatter intensity will be proportional to Z^2, leading to strong contrast between RE dopants and the alumina (or spinel) matrix. This has been observed at the grain boundaries of all RE-doped samples and can be attributed to RE segregation. It is further confirmed by the absence of increased grain boundary intensity in the HAADF image of the undoped spinel sample shown in Fig. 9. A long camera length was used to introduce diffraction contrast since no contrast was obtained at short camera lengths.

Intensity also varies with sample thickness (probability of scatter is proportional to thickness), which

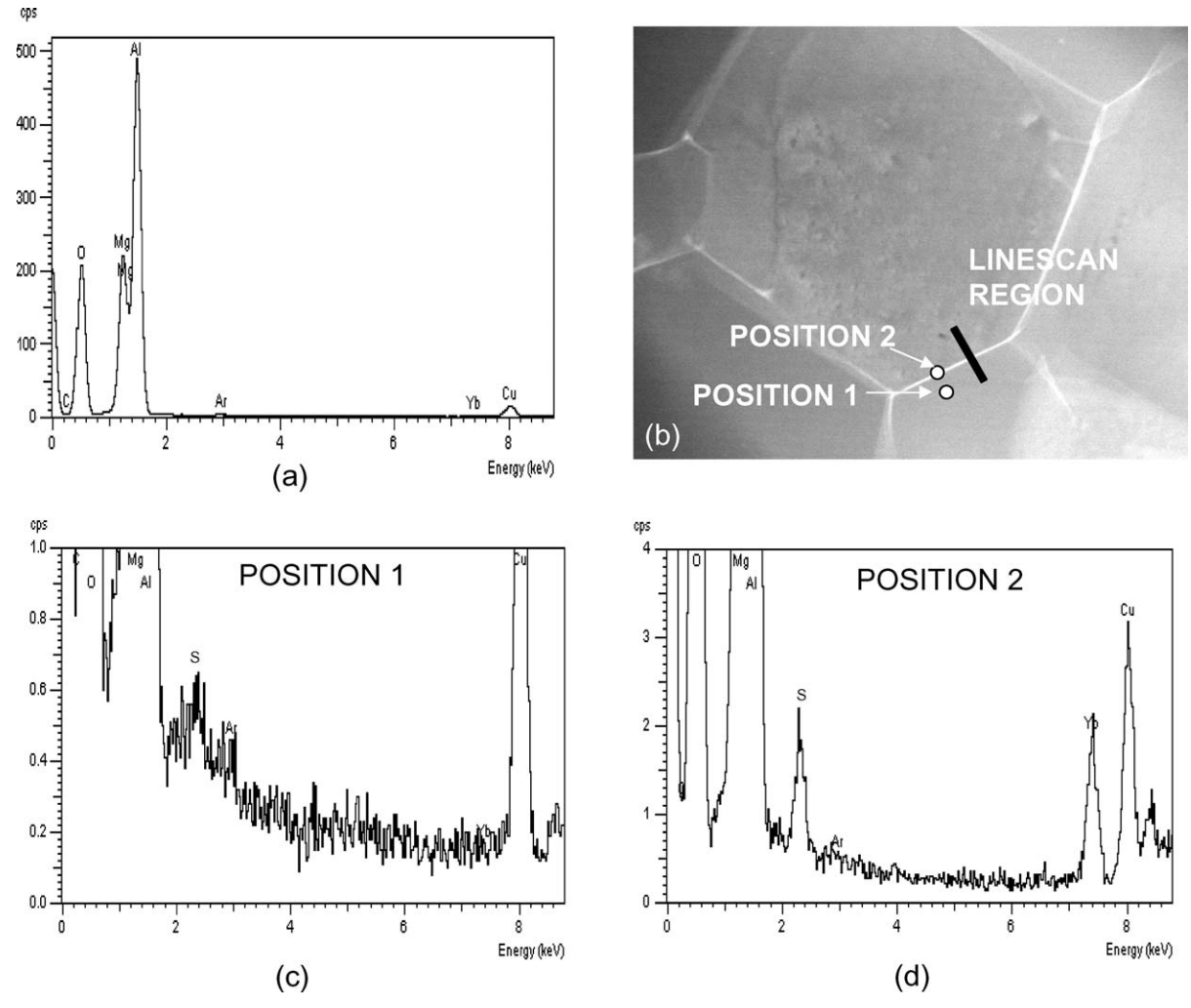

Figure 7 A bulk EDS spectrum of Yb doped spinel (a) acquired in the region of the HAADF image shown in (b). EDS spectra collected close to (c) and at (d) the grain boundary at locations indicated in (b).

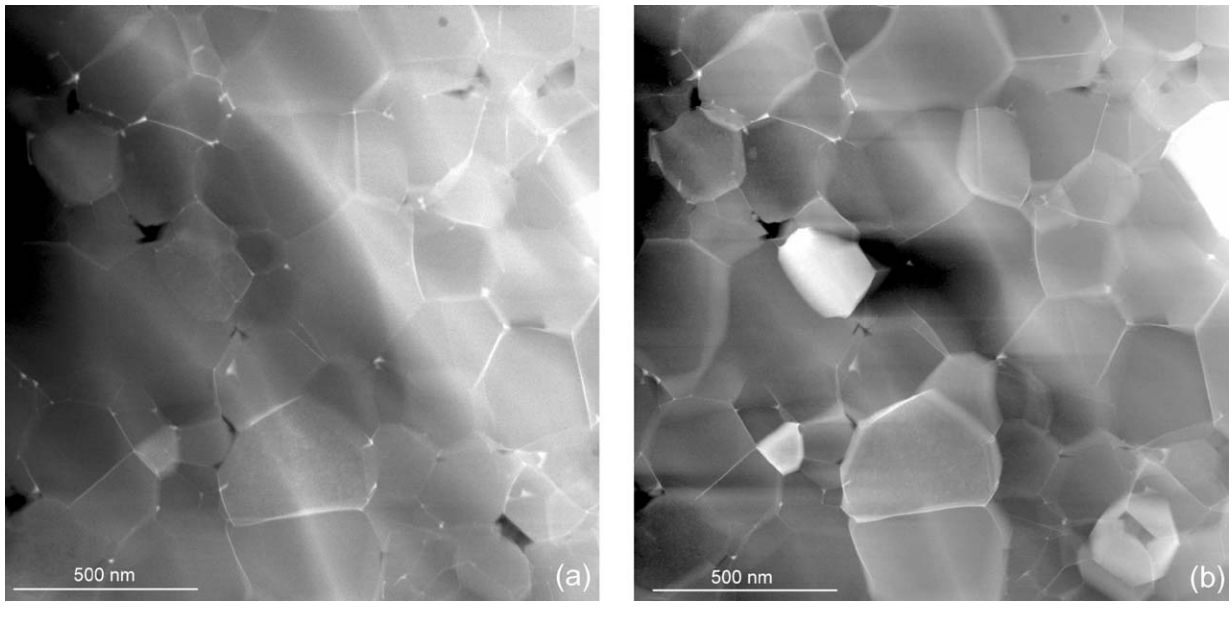

Figure 8 HAADF STEM micrographs of Gd-doped (500 ppm) spinel taken with collection angles of: (a) ∼50 mrad and (b) ∼20 mrad.

causes the observed gradual intensity gradient in images. Thus contrast in HAADF images occurs from local changes in atomic number density as well as sample thickness. It is interesting to note that atomic number and thickness have a similar effect on contrast in RE EDS elemental maps, Fig. 10 shows a comparison. The collection efficiency of the HAADF detector is however several orders of magnitude higher than the EDS detector. This has two major advantages. Firstly it enables the use of very small electron probes, which are necessary

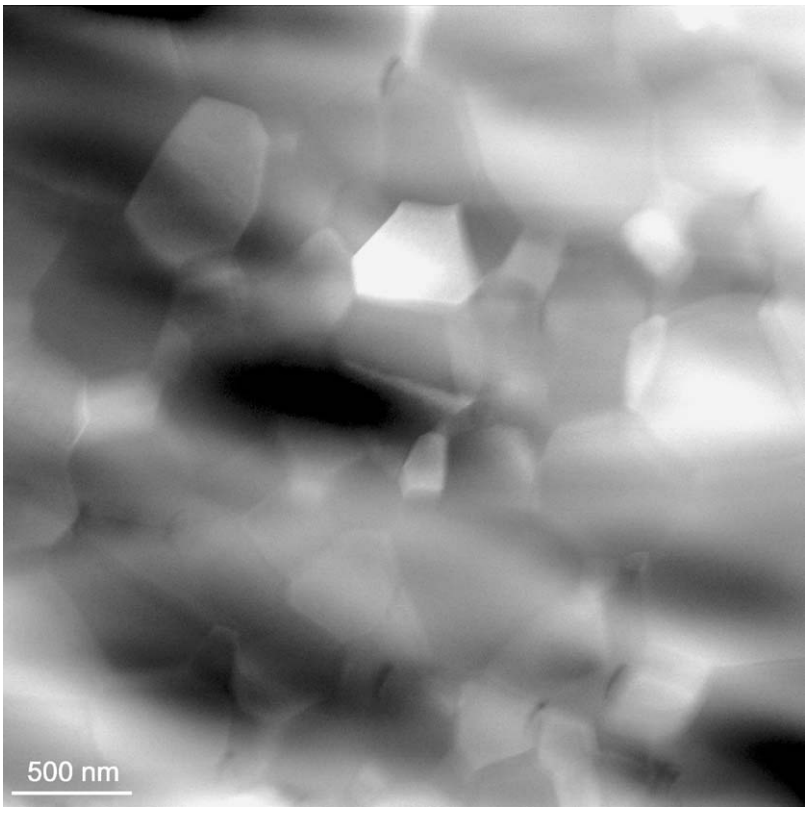

Figure 9 A HAADF STEM micrograph of undoped spinel (1400°C/10 min) taken with a low collection angle ∼20 mrad to reveal diffraction contrast.

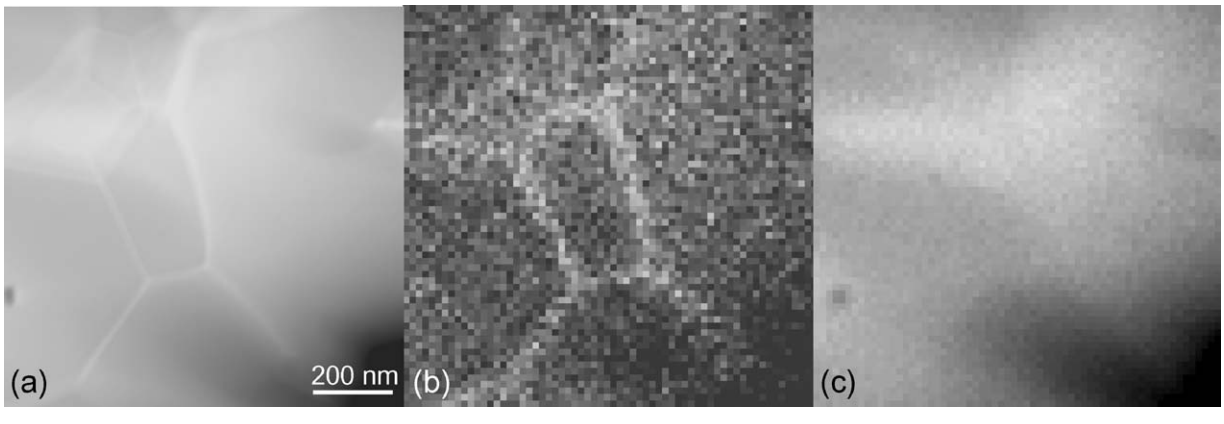

Figure 10 A comparison between a HAADF image (a) and a RE EDS elemental map (b) for La doped alumina. The Al EDS elemental map is shown in (c).

for high resolution but contain insufficient current for robust EDS. Secondly, since images are acquired in ∼5 s the effects of any sample drift are minimal. Pennycook [17] pioneered the technique of using HAADF images as high resolution elemental maps, and was able to quantify the intensity to an absolute accuracy of 20%. Similar quantification is possible for the RE-doped oxides studied in this project if the RE scattering cross section can be calculated. The actual relationship between Z and scattering is less than that predicted in Equation 1, due to increased electron shielding and general divergence from Rutherford Scatter with increasing Z. These two effects can be corrected by employing the Screened Rutherford Cross Section or (if $Z > 30$) the Mott Cross Section [16b]. At high Z it is particularly difficult to model such scattering for a real sample with reasonable accuracy and this will not be attempted. However, HAADF images can be used to provide high resolution elemental maps, which can be used to measure boundary thickness and enable a qualitative measure of RE content.

High magnification HAADF STEM images of grain boundaries were acquired from both RE-doped spinel and RE-doped alumina. In order to measure the thickness of the segregated layer, samples were tilted so that grain boundaries were viewed edge on. (The ability to tilt freely provides a significant advantage over EDS where the tilt allowed is restricted by detector position). The importance of aligning the grain boundaries in the precise edge on position is illustrated in Fig. 11, where the thickness of the grain boundary appears to vary. Image intensity profiles were acquired at various positions along the grain boundary. It was found that the thinnest region possesed a symmetric intensity

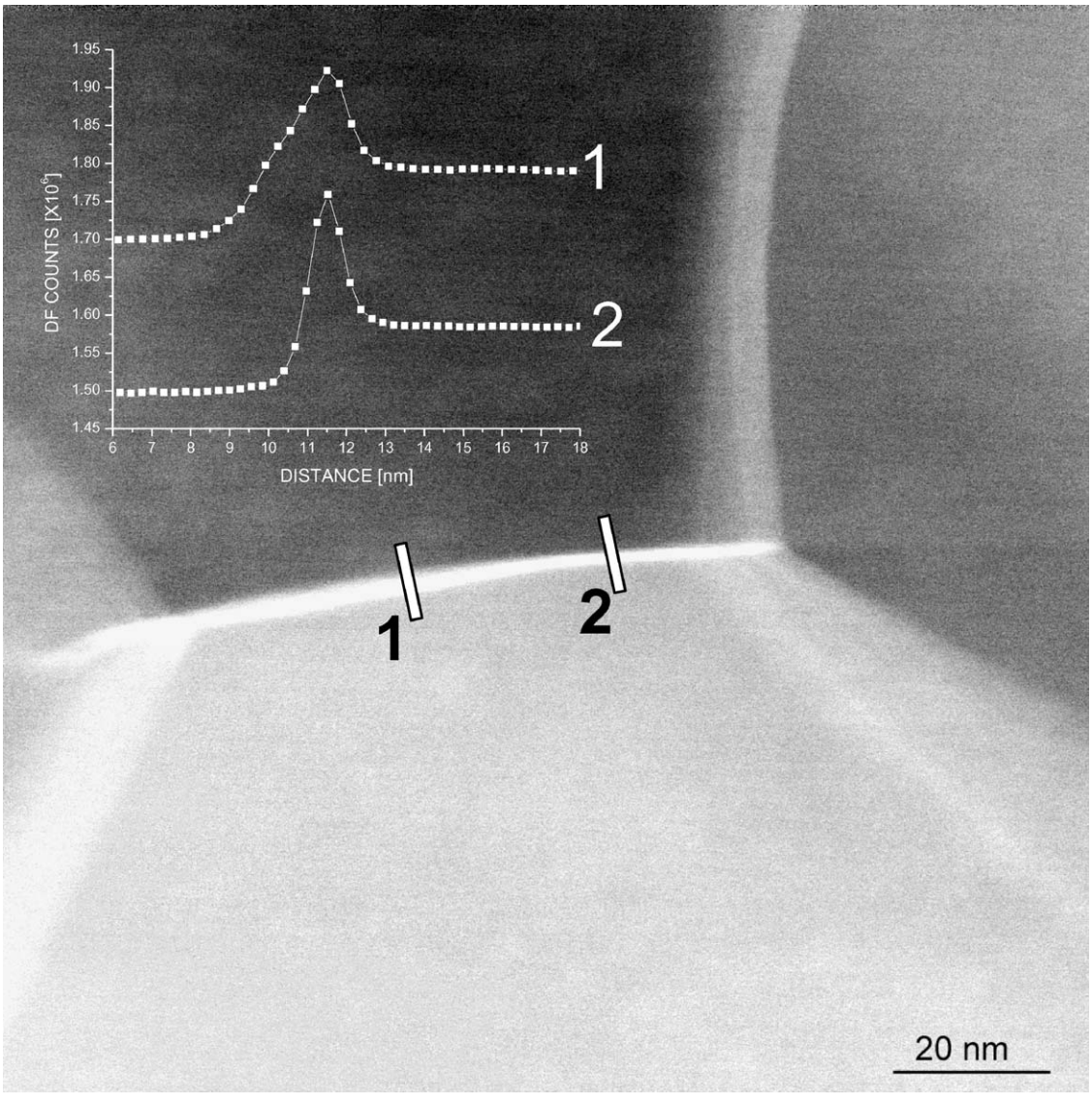

Figure 11 A high magnification HAADF STEM micrograph of a grain boundary in Gd-doped spinel. Inset is image intensity profiles of the grain boundary orientated near edge on (1) and edge on (2).

profile (profile 2), and as the boundary thickness appeared to increase so did the asymmetry (profile 1). Such image intensity profiles were used to align grain boundaries into a precise edge on position. The image in Fig. 11 was acquired with an intermediate collection angle (∼30 mrad) to balance the minimisation of noise and diffraction contrast. Fig. 9 demonstrates that diffraction contrast does not increase the intensity at grain boundaries and consequently the inclusion of some diffraction contrast does not alter the segregation profiles obtained.

The boundary thickness was similar throughout the sample suggesting segregation was not strongly dependent on grain boundary misorientation. The boundary thickness was also found to be similar for Yb, La and Gd dopants in both alumina and spinel. The FWHM of the intensity profile across the grain boundaries measured approximately 1 nm, which is similar to the size of the electron probe used. The measured width of the segregated layer is clearly compromised by the width of the smallest available electron probe, but can be considered to be $\leq$1 nm for all RE doped aluminas and spinels investigated (Yb, Gd, Eu and La).

3.5. Measuring RE concentration at grain boundaries using EDS and HAADF STEM

The grain boundaries analysed with HAADF STEM were subsequently analysed with EDS to enable the concentration of RE segregants to be quantified. Since the widths of segregating layers were determined from HAADF STEM images, high spatial resolution was not sought in EDS. This enabled the use of larger probes, resulting in increased statistical accuracy. Automated EDS linescans were performed perpendicular to edge on orientated grain boundaries. In these scans the location of the grain boundary is unambiguously shown in the image intensity profile, which is collected simultaneously with the X-ray derived chemical data. Since the electron probe is significantly larger than the segregated boundary layer the intensity profile provides a good and convenient measure of probe width. The image intensity profile can also allow the amount of drift (change of peak location) and contamination build up (change in profile shape) to be monitored.

Examples of typical EDS linescans for both an alumina and spinel sample are shown in Figs 12 and 13.

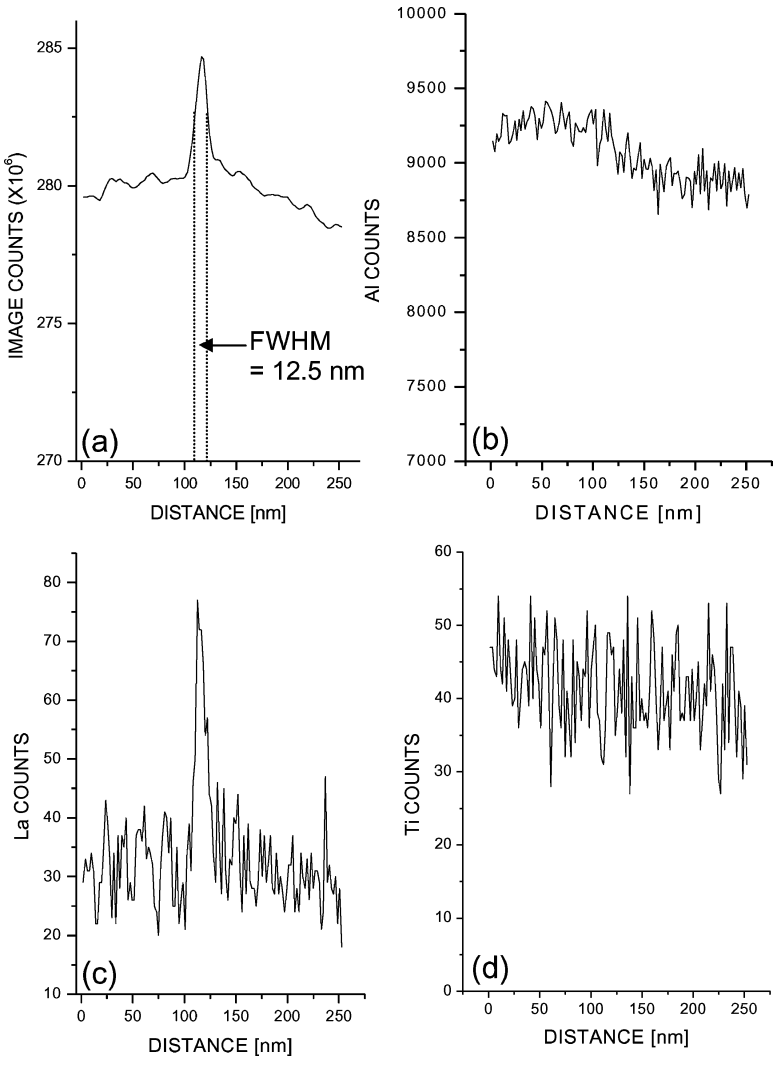

Figure 12 A typical EDS linescan obtained perpendicular to an edge-on orientated grain boundary in La-doped alumina. The image intensity variation (HAADF) (a) is compared with the EDS counts obtained for (b) Al, (c) La and (d) Ti.

The similarity in the contrast between HAADF images and RE elemental maps is once again underscored by the similarity in both position and shape of the image intensity and RE elemental profiles. In Fig. 12 the profile of Ti (an element not present in the sample) is included to show that background counts are constant across the scan length. The retention of stoichiometry across grain boundaries in spinel is shown by the constant Al/Mg ratio across the grain boundary region in Fig. 13d (the gradual reduction in this ratio is a thickness effect).

The measured value of the grain boundary thickness can be combined with EDS linescans to calculate segregant concentration at grain boundaries. This was done by calculating the fraction of the beam that is located on the grain boundary.

Fraction of beam on segregated layer

$$= \frac{2tr}{\pi r^2} = \frac{2t}{\pi r} \quad \text{when } 2r \gg t \tag{2}$$

where t is the thickness of the segregated layer at the grain boundary and $2r$ is probe diameter. The RE/Al ratio (for spinel samples RE/(Al + Mg) ratio) within the 1 nm segregated region was calculated assuming a RE:Al sensitivity factor of 0.53 for all samples (this factor was determined experimentally using a $LaAlO_3$ powder). Probe size was taken as the FWHM of the bright field intensity trace (e.g., from Figs 12a and 13a), which is valid provided $2r \gg t$. The RE/Al ratios for various samples are shown in Table I. The RE/Al ratio is the average of at least 3 boundaries in each sample, whereas the counts and probe size are typical values from the data set. The data shows no difference in the boundary concentration of Yb, Gd and La in alumina. This is consistent with the results of Bruley *et al.* who observed a similar RE grain boundary concentration for both Y and La using EDS and assuming a 1 nm segregated layer [15]. The Gd boundary concentration can be seen to be higher in doped spinel than alumina

TABLE I The RE/Al ratio at grain boundaries (assuming $t = 1$ nm) for selected samples

Sample	RE counts (after background subtraction)	Cation counts	Probe size (nm)	RE/Al ratio
La alumina	50	9000	12.5	0.10 ± 0.02
Gd alumina	23.5	2500	8	0.11 ± 0.02
Yb alumina	75	11700	12	0.11 ± 0.02
Gd spinel	80	3600	4.5	0.15 ± 0.02

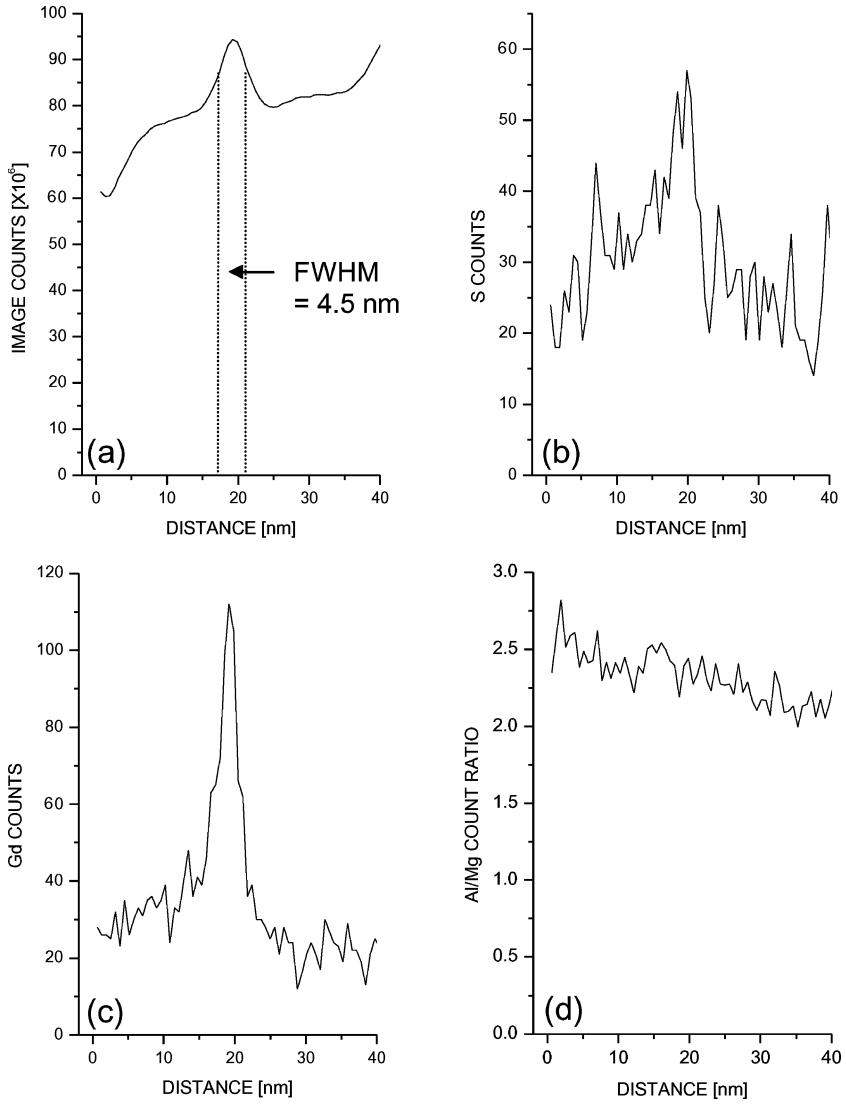

Figure 13 A typical EDS linescan perpendicular to an edge-on orientated grain boundary in Gd-doped spinel. The image intensity variation (HAADF) (a) is compared with the EDS counts obtained for S (b) and Gd (c). The Al/Mg ratio (d) shows the variation in cation stoichiometry.

(linescans for other doped spinels suggested a similar trend). Since the width of the segregated layer was assumed to be 1 nm (the upper limit), these boundary measurements provide the lower limit of RE segregant concentration.

The possibility that grain elongation in La-doped alumina was caused by a reduced concentration of segregant along the preferential growth direction was also briefly investigated. No evidence for this was found although concentration differences may only be present before La segregation reaches saturation. Elongated alumina grains may also be linked with the growth of elongated β-alumina ($LaAl_{11}O_{18}$) precipitates. The concentration of such precipitates was very low in the sample sintered at 1500°C and were easily differentiated from elongated matrix grains with the HAADF detector.

3.6. Aberration corrected STEM

Attempts to measure the width of the RE segregated region in the hybrid FEG TEM/STEM were compromised by the minimum size of electron probe available with sufficient probe current. This is dictated by the trade off between spherical aberration and diffraction/brightness, which are limiting when the convergence angle of the electron probe is large and small respectively. This trade-off has recently been removed by the development of spherical abberation correction in STEM. It is now possible to produce atom sized probes with an order of magnitude increase in current compared with uncorrected systems [18]. Fig. 14a–b shows HAADF images of a Eu-doped spinel (which exhibited similar segregation behaviour to other RE-doped spinels) formed with a 1 Å electron probe. The grain boundary aligned close to an edge-on position shows that the RE forms a continuous monolayer at the grain boundary. The image intensity profile shown in Fig. 14e shows that the boundary region has a width of ~0.4 nm. This value does however vary slightly along the boundary due to deviations from edge on-orientation caused by grain boundary curvature. The width of the Eu-rich layer was also seen to broaden due to electron probe induced Eu diffusion probably on the surface of the TEM section.

Grain boundary segregation was also examined using PEELS by studying the energy-loss near-edge structures (ELNES) of Al-L_1 and Eu $N_{4,5}$. Spectra were

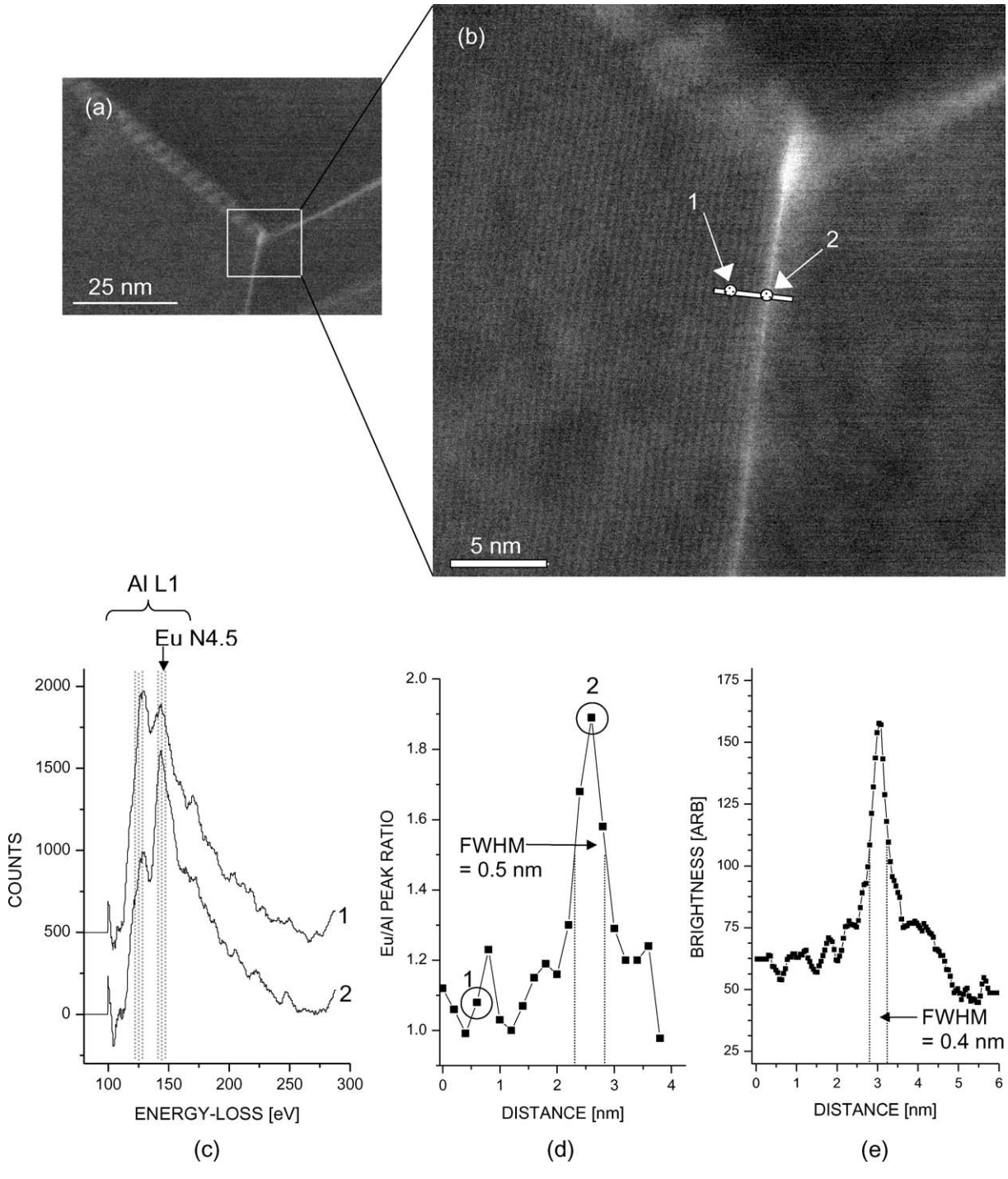

Figure 14 Ultra-high resolution HAADF images (taken with the superSTEM) of Eu-doped spinel (a–b). Examples of the ELNES spectra obtained close to (1) and on (2) the grain boundary. The integrated ratio of the peaks at 120–130 eV and 140–150 eV formed in a series of ELNES spectra taken across the grain boundary (d). The image intensity profile across the grain boundary is taken directly from the HAADF image (e).

acquired sequentially at 2 Å intervals along a line perpendicular to the grain boundary as shown in Fig. 14b.

The ELNES spectra obtained after background subtraction at and close to the grain boundary are compared in Fig. 14c. The fine structure is similar to that recorded from Al and Eu oxides. The relative intensity of the two main peaks can be seen to differ substantially between the two locations. However overlap between the Al-L_1 and Eu-$N_{4,5}$ edges means that although the peak located at ∼125 eV is characteristic of Al, that at ∼145 eV is due to a combination of Al and Eu. The change in concentration of Eu at the grain boundary was calculated simply from the integrated intensity ratio of these two peaks and is shown in Fig. 14d. Similar to the HAADF image, the PEELS shows that the Eu segregant is confined to within a 0.5 nm region at the grain boundary.

3.7. Grain boundary structure

Grain boundary structure was examined using HR-TEM. The number of boundaries that could be examined was limited by the difficulty of simultaneously aligning the boundary in the edge on position while achieving suitable diffraction conditions for lattice fringes either side of the boundary. Beam damage, particularly in alumina samples, limited exposure

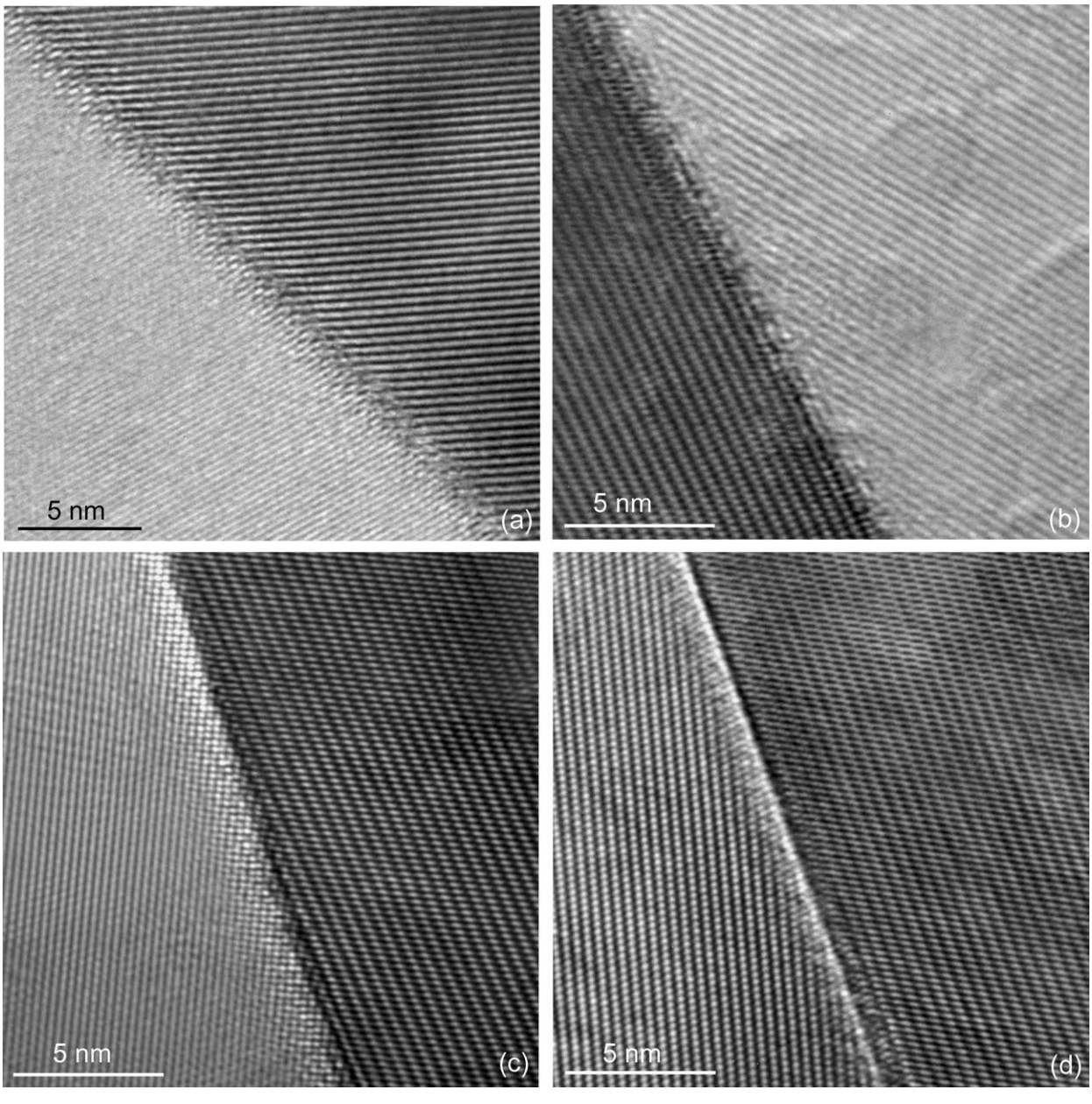

Figure 15 HRTEM micrographs of La-doped (a–c) and undoped (d) alumina grain boundaries viewed edge-on.

times to a few minutes thus inhibiting the alignment processes. Fig. 15a–c shows typical images acquired in randomly chosen grain boundaries in RE doped alumina (Fig. 15d shows a grain boundary of an undoped sample for comparison). The images show lattice fringes from neighbouring grains joining at the interface. These fringes become diffuse in the grain boundary region, which can be attributed to a relaxation in crystallographic structure near the grain boundary. This is consistent with experiments on bicrystals, which have shown that the addition of RE dopants have a tendency to broaden interfacial structure [19]. These studies also show that boundary structure and segregation behaviour are sensitive to the type of special boundary examined. The proportion of such special boundaries in RE-doped alumina is known to be very low (this is discussed further in Section 4), and the structure and chemistry of general boundaries are shown to be more uniform. Assuming that the RE cations are segregated uniformly in this 1 nm wide, less ordered grain boundary region, a distribution similar to Fig. 16 can be anticipated.

Fig. 17a shows a typical HR-TEM micrograph of a grain boundary interface in RE (Gd) doped spinel. Again there is no evidence of grain boundary phases and

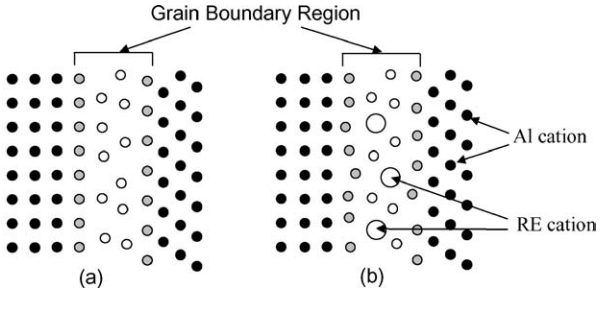

Figure 16 Schematic models of an undoped (a) and RE doped (b) grain boundary in alumina. Note the broader interfacial structure of the RE-containing grain boundary.

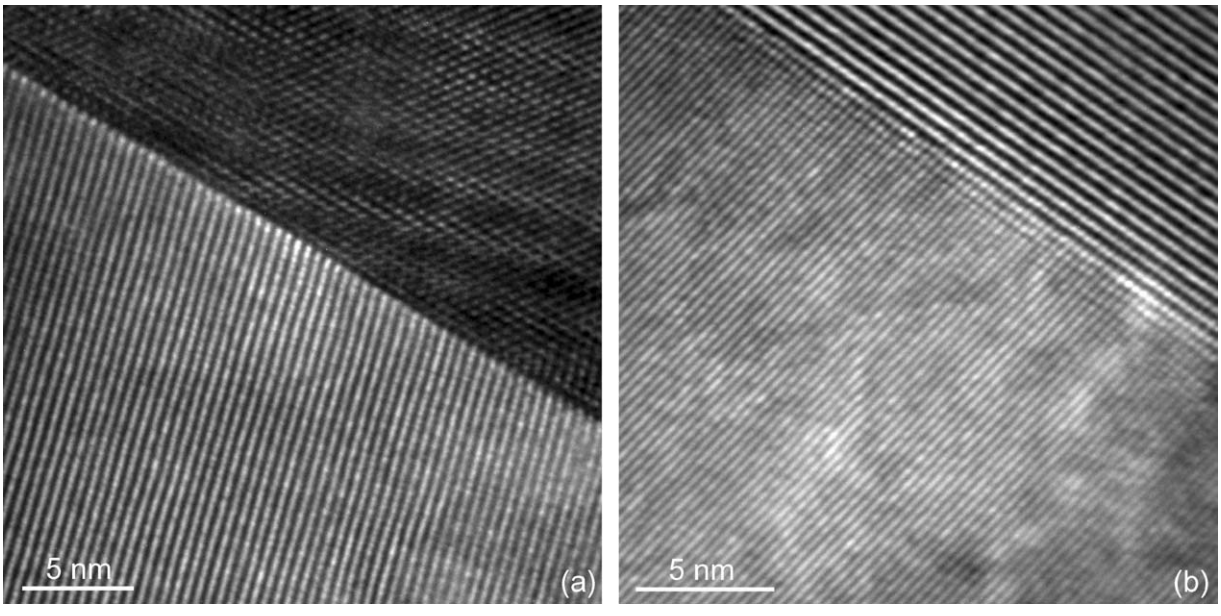

Figure 17 Typical HRTEM micrographs of Gd-doped spinel grain boundaries viewed edge on (a) and close to edge on (b).

the adjacent crystal structure is maintained to within a 0.5 nm separation. Increased brightness at the grain boundary can be attributed to the presence of segregants (this was insensitive to defocus). Fig. 17b shows that even when grain boundary orientation deviates slightly from the edge-on position, the crystal structures of the neighbouring grains are again maintained to within 0.5 nm of the grain boundary. HAADF STEM showed that RE segregants are also located within this grain boundary region. Together this is consistent with the RE cations occupying lattice sites adjacent to the grain boundary. In general grain boundaries this results in a continuous layer of segregant along the grain boundary. In special or low angle grain boundaries (the presence of which was confirmed during TEM investigations) the segregant distribution is expected to become discontinuous as low energy (or CSL) sites are filled with the appropriate matrix cation (Al or Mg).

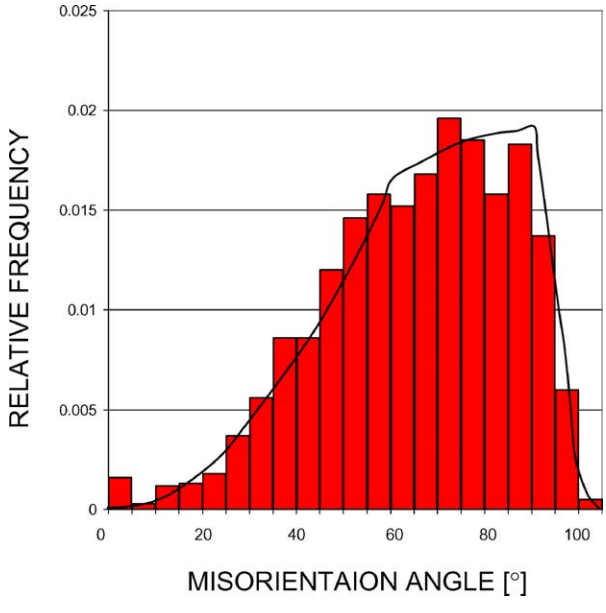

Figure 18 A histogram showing the misorientation distribution of Yb-doped alumina. Similar results were obtained for other doped and undoped aluminas.

4. Effect of grain orientation on surface topography

EBSD has been used to determine local grain orientation in a range of fine-grained alumina samples (undoped, Yb, Gd and La-doped). All samples were shown to possess near-random grain orientation and grain boundary misorientation distributions. A typical example of the latter is compared with the theoretical random distribution in Fig. 18. The proportion of special CSL grain boundaries was also found to be very low. This is consistent with the results of Cho *et al.* [20] who studied the effect of RE addition on grain boundary character in similar systems albeit with different dopant chemistries and (in general) coarser-grained microstructures.

A typical example of an EBSD pattern is shown in Fig. 19. The average pattern quality was however found to decrease significantly as the average grain size of the sample is reduced below 1 μm. This is partly due to the increased grain boundary area, which causes an intrinsic reduction in pattern quality. This is however exacerbated by pattern overlap, which occurs in near grain boundary regions, and shadowing caused by grain height variations (the grain height variation were insensitive to grain size and hence became more problematic as grain size was reduced). The relationship between crystallographic orientation and grain height variation is discussed in the next section.

4.1. The relationship between wear rate and crystal orientation

Polishing alumina with (alkaline) colloidal silica produces a surface with minimal strain (suitable for EBSD) but relatively rough due to grain height variations. These grain height variations provide sufficient

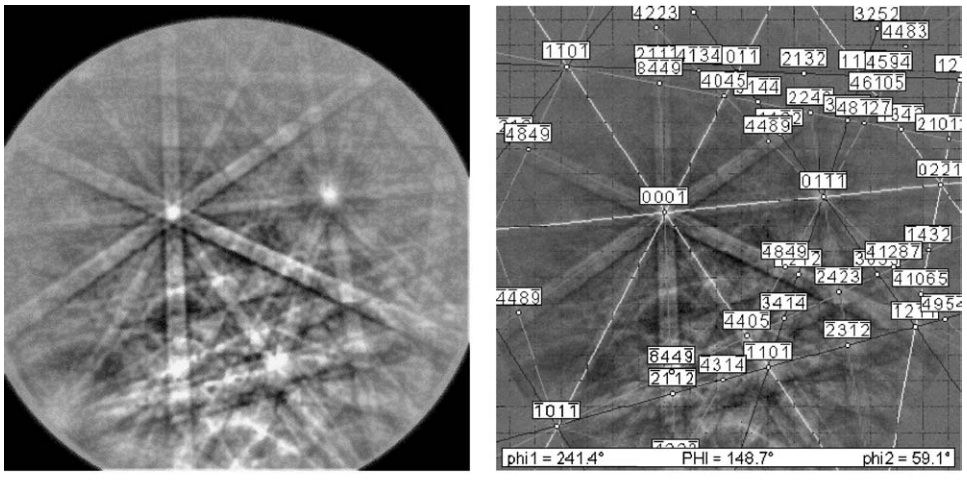

Figure 19 A typical EBSD pattern of alumina without (a) and with (b) the bands used for orientation determination displayed.

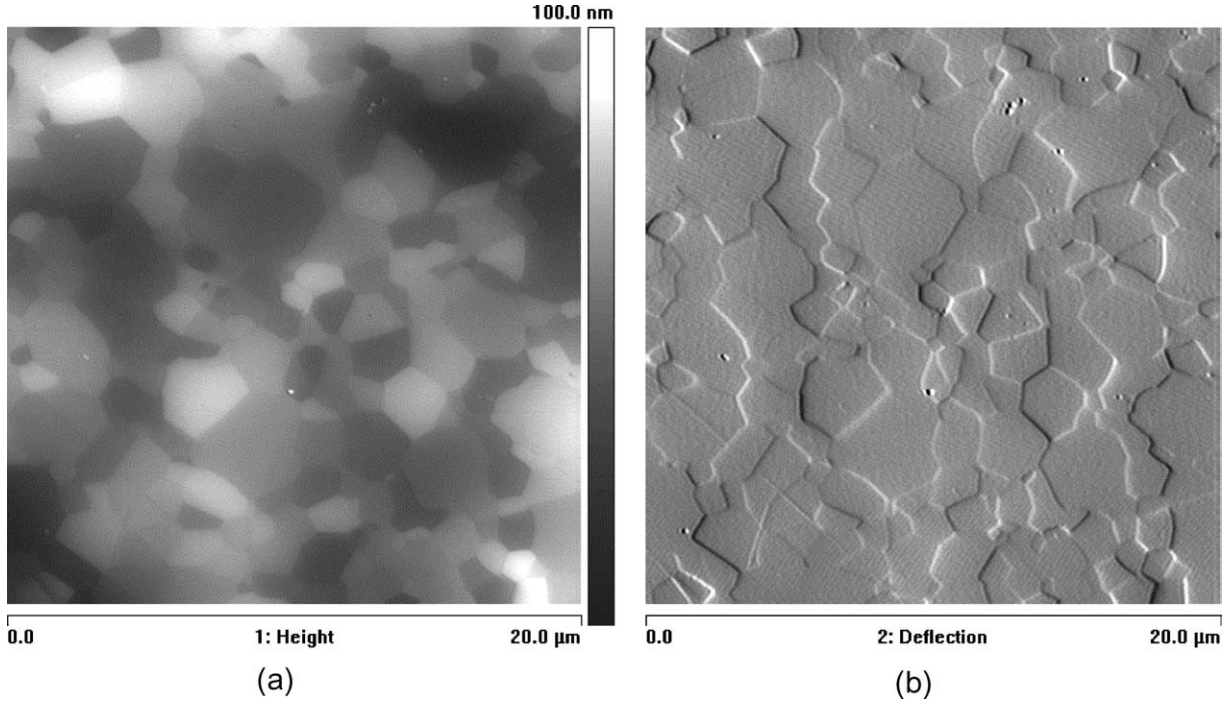

Figure 20 AFM images acquired in contact mode of Yb-doped alumina. Images were formed from the height (a) and deflection (b) signals.

topographic contrast to reveal grain microstructure with visible light microscopy, SEM or AFM. AFM is particularly suited to fine-grained oxide ceramics because it combines a high-resolution capability with the ability to quantify roughness and other surface features. Also poor electrical conductivity is not an issue as it is in SEM, although conductive coating can be avoided in modern SEMs by operating at either low voltage or low vacuum. In AFM, images can be formed from a variety of signals produced from sample-tip interactions. Fig. 20 shows height (a) and deflection (b) images, for a fine-grained Yb-doped alumina taken in contact mode. The height image provides quantitative height information whilst the deflection signal produces an image, which is in effect the derivative of the height image, with a natural 3D effect enabling easier visualisation of grain microstructure (height images can also be displayed in 3D format e.g., Fig. 23).

The rate of grain wear during chemo-mechanical polishing is dependent on the crystallographic orientation of the grain, which leads to the observed grain height variation. The orientation of the grains in the AFM image in Fig. 20 are shown in the EBSD derived inverse pole figure image map in Fig. 21a. Grain orientations are displayed relative to the sample surface plane and are colour coded according to the stereographical triangle shown in Fig. 21c. Comparison of Figs 20 and 21 shows that grains orientated close to the 0001 plane are recessed. This is shown more clearly in Fig. 21b where all grains within a 30° tolerance of the 0001 plane are indicated. The wear rate of other planes was found to be more sensitive to the precise crystallographic orientation. EBSD possesses a high level of accuracy in

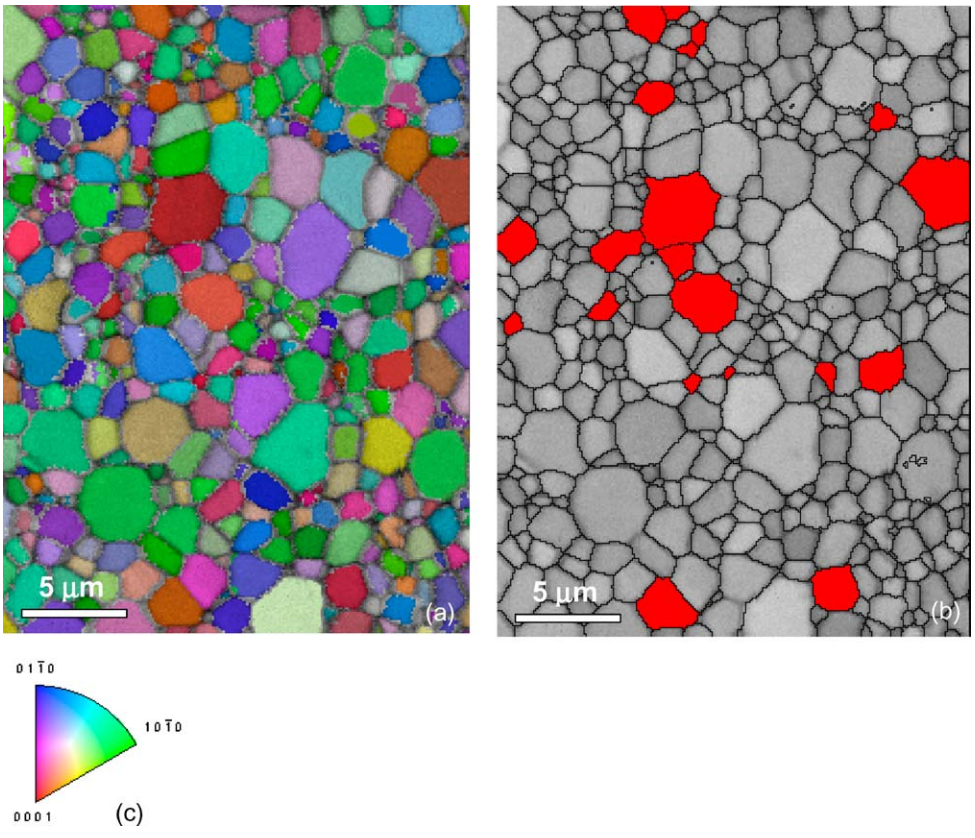

Figure 21 EBSD derived image maps of Yb-doped alumina showing grain orientation with image quality overlay (a) and grains located within a 30° tolerance of the 0001 plane. The grain colours shown in (a) are related to orientation with the stereographical triangle in (c).

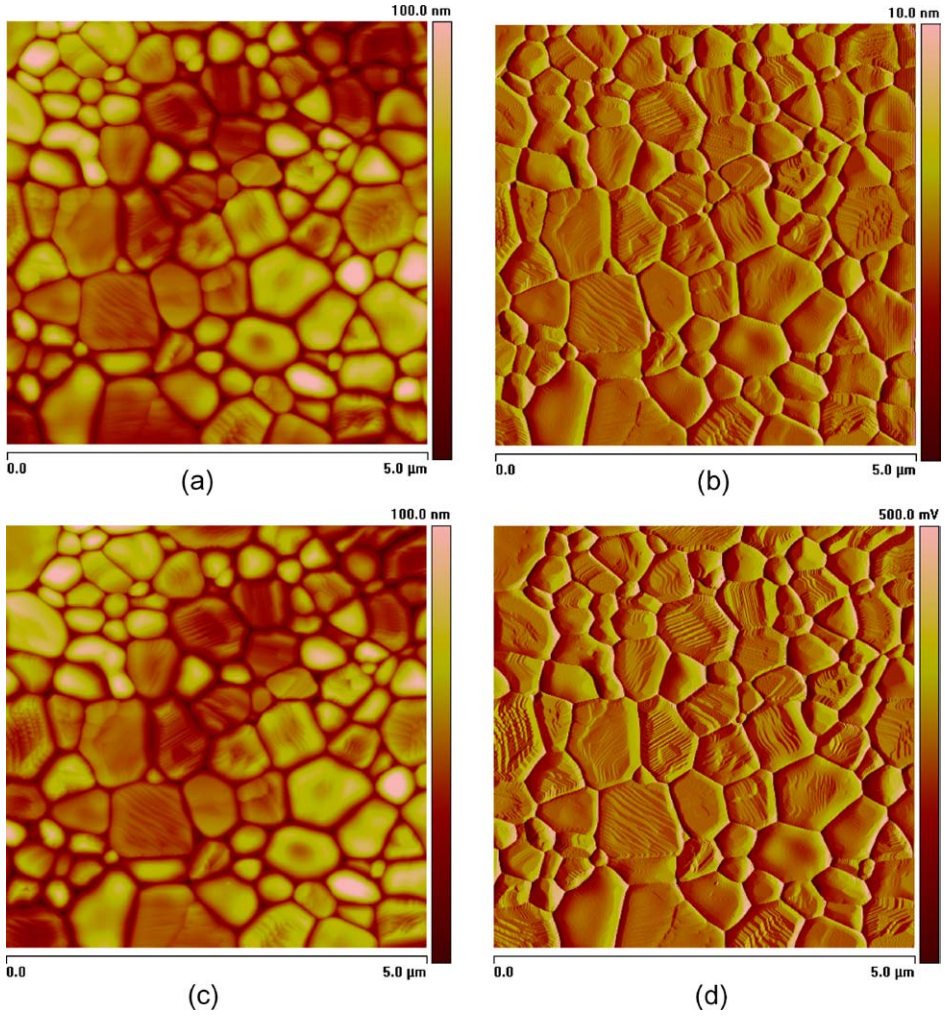

Figure 22 A comparison between contact (a–b) and tapping images (c–d) of thermally etched fine-grained alumina.

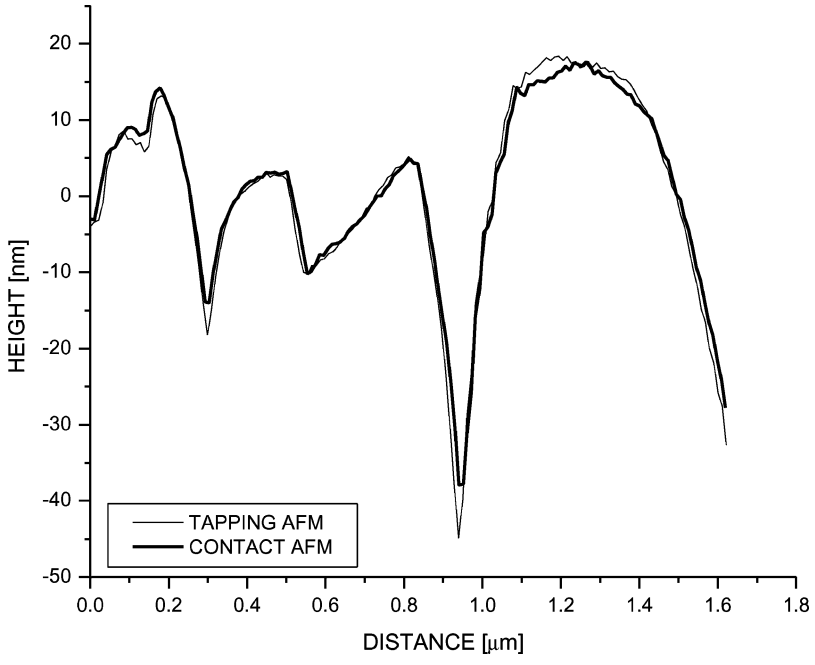

Figure 23 A comparison of the trace profiles produced from contact and tapping along the same section of sample.

orientation measurement (absolute orientation typical within $\sim 2^{\circ}$) and together with AFM, it is possible to relate grain wear with orientation over all possible orientations, although this would require the examination of a very large number of grains.

This method of linking grain wear to orientation could be extended to other wear situations. For example alumina on alumina wear under mild conditions is often tribochemical and also leads to grain height variations [21, 22]. If the process controlling wear rate is the same (e.g., surface adsorption) as colloidal silica on alumina, then a similar relationship between wear and orientation is expected.

4.2. Using AFM to examine thermally etched samples

The use of AFM to study thermal grooves at grain boundaries is becoming a popular alternative to the traditional and significantly more labour-intensive Metal (or Carbon) Reference Line technique and Optical Interferometry. In addition to increased speed of measurement AFM also offers a significant improvement in resolution, which enables materials with fine grain sizes ($<2\ \mu$m) to be investigated. The majority of studies reported in the literature, which use AFM to examine thermal grooves in metallic systems, use a Si_3N_4 tip in contact mode. The main attraction of the Si_3N_4 tip is that it is fairly robust allowing large areas to be scanned quickly. However, the major drawback of Si_3N_4 tips are that they are relatively coarse, possessing a truncated cone shape with a polished point typically with a diameter between 50 and 60 nm [23, 24]. This tip geometry introduces two well-known errors into the surface profile obtained. Firstly the cone shape (inner angle typically 35°) causes flat stepped regions to appear curved [25] and secondly the width of the tip limits the thickness of grooves that can be accurately examined to $>2\ \mu$m [23]. A further problem with AFM when performed on hard materials such as alumina is tip wear. This is a significant problem when quantitative measurements are required as tip wear increases the width of the point in contact with the sample. Tip wear is expected to increase as force, tip velocity and scan size are increased (i.e., as grain size is increased). To enable the boundary grooves of fine-grained ($<2\ \mu$m) materials to be studied an alternative Si tip was used in tapping mode. The decreased hardness of the Si tip is offset by the use of the tapping mode, in which only transient contact with the sample is made. Tip wear was found to be minimal if operation was performed under optimal conditions (i.e., minimal tip sample forces). This is in contrast with the severe tip wear encountered when using a Si tip in contact mode as has been reported previously by Saiz *et al.* [26]. Fig. 22 compares images that have been acquired in the same area of a sample in both Contact (with Si_3N_4) and Tapping (with Si tip) modes. Although the images look similar, the cross sectional profile shown in Fig. 23 shows that in tapping mode the tip penetrates deeper into the thermal groove. Also, the higher magnification images in Fig. 24 demonstrate the improved resolution obtained in tapping mode. An example of a high resolution AFM image of fine-grained undoped alumina is shown in both conventional 2D and 3D formats in Fig. 25. The 3D representation provides a particularly good illustration of grain (and grain-boundary) curvature, faceting and grain height variation.

4.3. Effect of misorientation and dopant on groove size

AFM images and the corresponding grain boundary misorientation map (from EBSD) for undoped and Yb-doped alumina are compared in Fig. 26. The locations of the thermal grooves in the AFM images are in excellent agreement with the grain boundaries within the

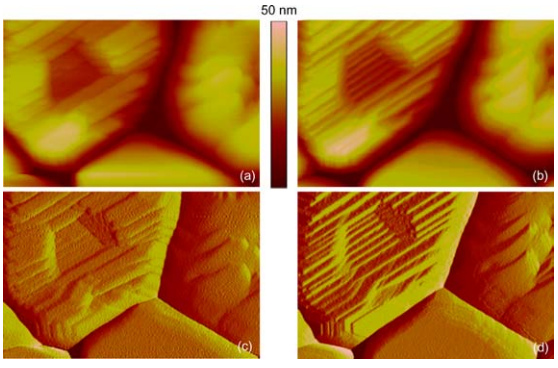

Figure 24 A comparison of high magnification images obtained from contact (a and c) and tapping (b and d). (Image width 800 nm.)

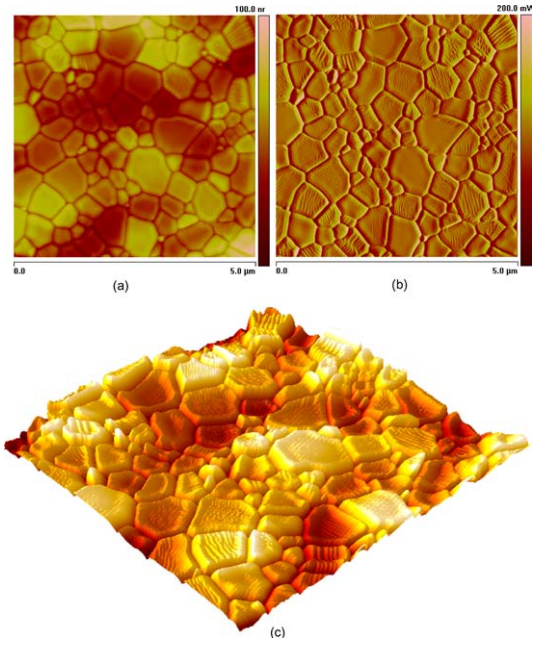

Figure 25 High-resolution AFM images of an etched fine-grained Al_2O_3 acquired using a Si tip in tapping mode. The images were produced from height (a and c) and amplitude (b) data ((c) is a 3D representation of (a)).

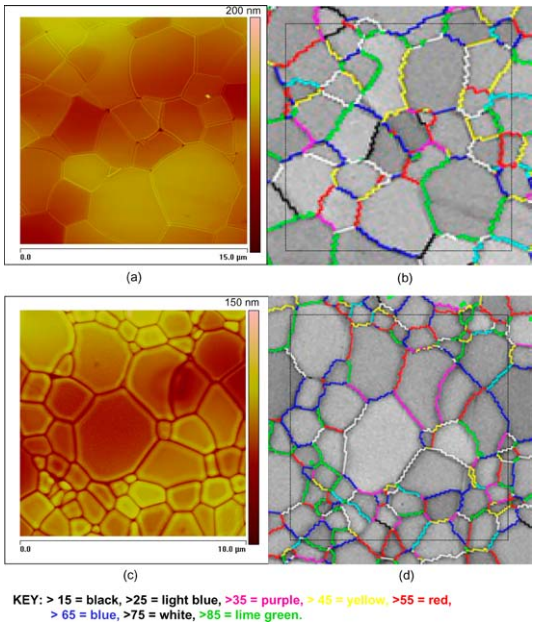

Figure 26 AFM images (a and c) and EBSD derived grain boundary misorientation maps (b and d) collected at the same location in undoped (a and b) and Yb doped (c and d) Al_2O_3.

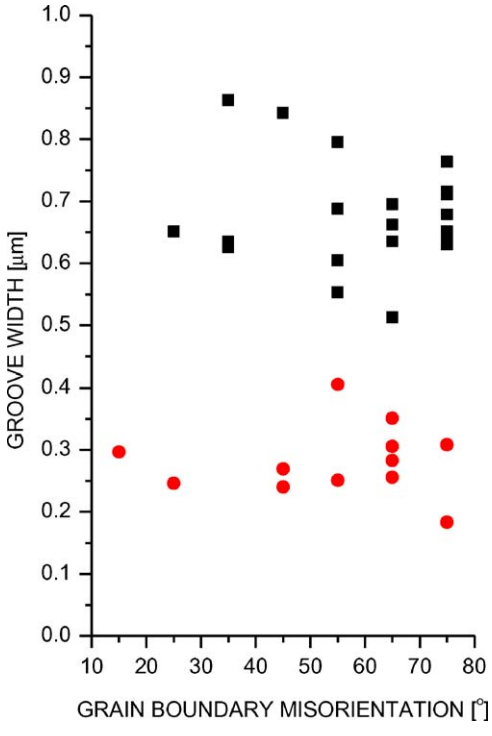

Figure 27 A scatter graph comparing the groove width of undoped (grey) and Yb-doped (black) Al_2O_3 as a function of misorientation.

corresponding EBSD map. The size of the grooves is relatively constant which is consistent with the very low fraction of special and low-angle boundaries determined using EBSD. This is confirmed in Fig. 27, which shows that grain boundary misorientation has no discernable effect on groove size (shown as groove width but similar profiles were obtained for groove depth) for either doped or undoped samples. The Yb-doped sample can also be seen to possess much larger grooves than the undoped sample. Other (Gd and La) dopants were found to have a similar effect on groove size. This is not unexpected because groove geometry is known to be highly sensitive to the presence of segregating impurities [27]. The large increase in groove size of doped samples must be related to the out-diffusion of RE segregants to the free surface. Consequently groove size can be linked with RE concentration at the grain boundary. This relationship can be used, for example, to determine the grain size at which grain boundary saturation occurs for a particular system. Taking quantitative measurement from the thermal grooves in such fine-grained samples is however hindered by a number of practical issues. These include the random orientation of the grain boundary plane, surface anisotropy, faceting on both grains and thermal grooves and the effect of grain size on groove geometry (groove width and hence depth are increasingly constrained as grain size is decreased).

The out diffusion of RE segregants from the grain boundary to the free surface results in unreliable measurements of grain boundary energy or energy anisotropy. This is because the out-diffusion of dopants to the free-surface, apart from boundary-depletion, has a more sensitive influence on the surface energy. This modifies the balance between surface and grain

boundary energy, which is routinely used for grain boundary energy calculations. This has important implications for all studies measuring grain boundary energy in samples possessing grain boundary segregants.

5. Conclusions

A wide range of techniques are available to characterise fine-grained ceramic materials. Of these, TEM based techniques are particularly valuable in studying grain boundary structure and quantifying segregation. These techniques have shown that the RE segregant is confined to within a 1 nm wide region at the grain boundary in both alumina and spinel. Assuming that segregation occurs in a 1 nm wide region, the RE concentration is 10 and 15% of the cation total in alumina and spinel respectively, and is insensitive to the identity of RE cation.

A new level of imaging and analytical performance has recently become available with the development of spherical aberration correction in STEM. These microscopes possess atomic resolution imaging (HAADF) coupled with a single atom analytical detection capability (PEELS). Ultra-high resolution HAADF STEM and PEELS showed that in Eu doped spinel the segregated region was <0.4 nm wide, and consisted of a single layer of Eu atoms at the grain boundary. The RE concentration in this single layer is expected to be approximately 50% of the cation total from EDS studies. Further ultra-high resolution STEM is planned to study a wider range of grain boundaries in both RE-doped alumina and spinel systems.

EBSD showed that the addition of dopants had negligible effect on either the grain orientation distribution (texture) or the concentration of special grain boundaries in alumina. Also, no correlation was observed between grain boundary segregation and misorientation. The thermal grooves formed in RE-doped alumina were much larger than those formed in undoped samples due to out diffusion of RE atoms to the surface. This process reduces the surface energy of the system and consequently alters the energy balance often used in grain boundary energy calculations.

AFM in tapping mode can provide HR-images of thermally etched samples with a more accurate profile of the groove root compared with the traditional contact mode. Tapping mode requires slower scan speeds and is consequently only suitable for fine-grained materials.

EBSD in conjunction with AFM has been used to relate grain orientation with wear rate anisotropy in fine-grained alumina. Grain surfaces close to the (0001) plane were found to exhibit high wear, whilst other orientations were found to be much more sensitive to grain orientation.

Although grain boundary segregation is beneficial for grain-size control, sinterability and mechanical properties, there may be greater susceptibility to grain boundary embrittlement resulting from a reduction in intergranular fracture surface energy which dominates the reduction in grain boundary energy. At high temperatures, increased grain boundary groove size due to thermal etching in doped ceramics may also contribute to the critical defect population and a limit to fracture stress in high strength materials.

Acknowledgments

This research was supported by the European Community under the 'Competitive and Sustainable Growth' programme (Contract Number G5RD-CT-1999-00052) and EPSRC. The Authors wish to acknowledge Dr. A. Bleloch for superSTEM operation, N. R. Wilson for assisting with AFM, and F. J. Humphreys and I. Brough (UMIST) and R. de Kloe (TSL) for access to EBSD systems.

References

1. K. HAYASHI, O. KOBAYASHI, S. TOYODA and K. MORINAGA, *Mater. Trans. JIM* **32** (1991) 1024.
2. R. APTEZ and M. P. B. VAN BRUGGEN, *J. Amer. Ceram. Soc.* **86** (2003) 480.
3. A. KRELL, *Mater. Sci. Eng.* A **245** (1998) 277.
4. S. LARTIGUE, L. PRIESTER, F. DUPAU, P. GRUFFEL and C. CARRY, *ibid.* A **164** (1993) 211.
5. J. CHO, C. M. WANG, J. M. RICKMAN and M. P. HARMER, *Acta Mater.* **47** (1999) 4197.
6. Y. M. CHIANG and W. D. KINGERY, *J. Amer. Ceram. Soc.* **72**(2) (1989) 271.
7. S. WILKES, *Mater. World* **11**(3) (2003) 23.
8. J. K. FARRER, J. R. MICHAEL and C. B. CARTER, in "Electron Backscatter Diffraction in Materials Science," edited by A. J. Schwartz, M. Kumar and B. L. Adams (Kluwer Academic, 2000) p. 299.
9. G. D. WEST, J. M. PERKINS and M. H. LEWIS, *Key Eng. Mater.* **264–268** (2004) 801.
10. A. M. THOMPSON, K. K. SONI, H. M. CHAN, M. P. HARMER, D. B. WILLIAMS, J. M. CHABALA and R. LEVI-SETTI, *J. Amer. Ceram. Soc.* **80**(2) (1997) 373.
11. R. F. COOK and A. G. SCHROTT, *ibid.* **71** (1988) 50.
12. M. A. GÜLGÜN, R. VOYTOVYCH, I. MACLAREN, M. RÜHLE and R. M. CANNON, *Interf. Sci.* **10** (2002) 99.
13. C. M. WANG, G. S. CARGILL III, H. M. CHAN and M. P. HARMER, *Acta Mater.* **48** (2000) 2579.
14. H. YOSHIDA, Y. IKUHARA and T. SAKUMA, *ibid.* **50** (2002) 2955.
15. J. BRULEY, J. CHO, H. M. CHAN, M. P. HARMER and J. M. RICKMAN, *J. Amer. Ceram. Soc.* **82**(10) (1999) 2865.
16. D. B. WILLIAMS and C. B. CARTER, "Transmission Electron Microscopy" (Plenum, New York, 1996)(a)p600, (b) p40.
17. S. J. PENNYCOOK, *Annu. Rev. Mater. Sci.* **22** (1992) 22.
18. O. L. KRIVANEK, N. DELBY and A. R. LUPINI, *Ultramicroscopy* **78** (1999) 1.
19. T. GEMMING, S. NUFER, W. KURTZ and M. RÜHLE, *J. Amer. Ceram. Soc.* **86**(4) (2003) 590.
20. J. CHO, C. M. WANG, H. M. CHAN, J. M. RICKMAN and M. P. HARMER, *J. Mater. Sci.* **37** (2002) 59.
21. A. RAVIKIRAN, *J. Mater. Sci. Lett.* **19** (2000) 1041.
22. *Idem.*, *Tribol. Trans.* **43** (2000) 287.
23. D. M. SAYLOR and G. S. ROHRER, *J. Amer. Ceram. Soc.* **82**(6) (1999) 1529.
24. W. SHIN, W. S. SEO and K. KOUMOTO, *J. Eur. Ceram. Soc.* **18** (1998) 595.
25. U. D. SCHWARZ, H. HAEFKE, P. REIMANN and H. GUNTERODT, *J. Microscopy* **173**(3) (1994) 183.
26. E. SAIZ, R. M. CANNON and A. P. TOMSIA, *Acta Mater.* **47**(15) (1999) 4209.
27. J. M. DYNYS, R. L. COBLE, W. S. COBLENZ and R. W. CANNON, in "Sintering Processes," edited by G. C. Kuczynski (Plenum Press, New York, 1980) p. 391.

Received 20 December 2003
and accepted 20 January 2004